Volume 1
Number 9
December 2020
Pages 3075–3608

Materials Advances

rsc.li/materials-advances

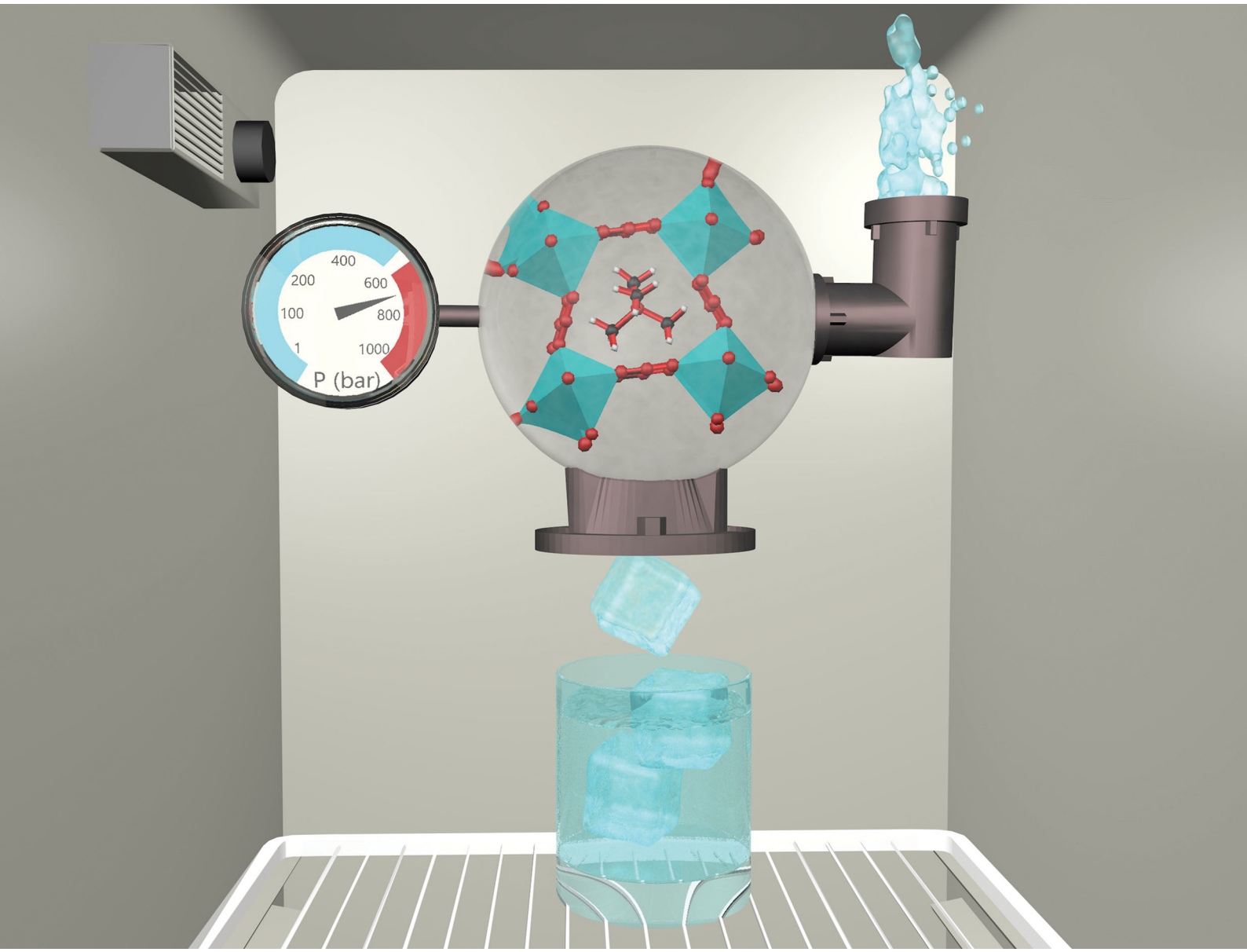

ISSN 2633-5409

ROYAL SOCIETY OF CHEMISTRY

COMMUNICATION

María Antonia Señarís-Rodríguez, Xavier Moya, Juan Manuel Bermúdez-García *et al.*

Near-room-temperature reversible giant barocaloric effects in $[(CH_3)_4N]Mn[N_3]_3$ hybrid perovskite

Materials Advances

ROYAL SOCIETY OF CHEMISTRY

COMMUNICATION

View Article Online
View Journal | View Issue

Cite this: *Mater. Adv.*, 2020, **1**, 3167

Received 29th August 2020,
Accepted 24th September 2020

DOI: 10.1039/d0ma00652a

rsc.li/materials-advances

Near-room-temperature reversible giant barocaloric effects in $[(CH_3)_4N]Mn[N_3]_3$ hybrid perovskite†

Jorge Salgado-Beceiro, [a] Ariel Nonato, [b] Rosivaldo Xavier Silva, [c] Alberto García-Fernández, [a] Manuel Sánchez-Andújar, [a] Socorro Castro-García, [a] Enric Stern-Taulats, [d] María Antonia Señarís-Rodríguez, *[a] Xavier Moya *[d] and Juan Manuel Bermúdez-García *[ad]

We report giant reversible barocaloric effects in $[(CH_3)_4N]Mn[N_3]_3$ hybrid organic–inorganic perovskite, near its first-order cubic-monoclinic structural phase transition at $T_0 \sim 305$ K. When driving the transition thermally at atmospheric pressure, the transition displays a large change in entropy of ~ 80 J K^{-1} kg^{-1} and a small thermal hysteresis of ~ 7 K, as well as a large change in volume of $\sim 1.5\%$. When driving the transition with pressure near room temperature, the transition displays large changes in entropy of ~ 70 J K^{-1} kg^{-1}, which represent a giant barocaloric response. Hybrid perovskites with similar barocaloric response and lower operating temperatures may find applications in environmentally friendly cooling.

In recent years, barocaloric materials have arisen as promising solid-state replacements to commercial refrigerant fluids, which are strong volatile greenhouse contributors that are often flammable or toxic.[1–3] Similarly to refrigerant fluids, barocaloric materials display large thermal changes under application and removal of hydrostatic pressure, which are typically parameterised as pressure-driven isothermal changes in entropy ΔS, or pressure-driven adiabatic changes in temperature ΔT.[1] However, due to their solid nature, barocaloric materials ultimately represent an environmentally friendly cooling solution.

With this motivation, a number of materials families have been investigated for barocaloric applications, which include magnetic alloys,[4–9] polymers,[10] oxyflourides,[11–14] ferroelectric oxides,[15,16] ferrielectric salts,[17] superionic conductors,[18,19] plastic crystals,[20–23] and hybrid organic–inorganic perovskites.[24–26] The latter have the potential to operate at hydrostatic pressures that are similar to those available in commercial compressors (≤ 150 bar), specifically in the case of dicyanamide hybrid perovskites.[24,25] Moreover, hybrid perovskites have the advantage that they can be synthesized using fast, economic, simple and escalable methods, and their chemical composition can be easily modified by using different building-blocks, which can lead to an optimization of their barocaloric parameters depending on the application of interest.[26]

Dicyanamide perovskites have been shown to display giant barocaloric effects only at temperatures well above room temperature (≥ 330 K).[24,25] Here we bring the operating temperature of hybrid perovskites closer to room temperature, by demonstrating giant barocaloric effects in a $[(CH_3)_4N]Mn[N_3]_3$ azide perovskite at ~ 310 K and above. Near its non-isochoric cubic ($Pm\bar{3}m$) to monoclininc ($P21/m$) phase transition,[27,28] we find pressure-driven entropy changes $|\Delta S|$ of ~ 70 J K^{-1} kg^{-1} that can be driven reversibly using changes in applied pressure p of $|\Delta p| = |p - p_{atm}| \sim |p| \sim 1$ kbar (p_{atm} is atmospheric pressure). Our results improve upon the performance of state-of-the-art barocaloric hybrid perovskites, by increasing twofold or more the barocaloric entropy change, and decreasing operating temperatures by ~ 25 K or more, at the expense of larger driving pressures.

Colourless polycrystalline powders of $[(CH_3)_4N]Mn[N_3]_3$ were synthesised *via* liquid diffusion.[27,28] 0.5 M of NaN_3 and 0.5 M of $[(CH_3)_4N]Cl$ were dissolved in a 1 : 1 mixture of methanol : water of volume 2.5 mL, in a glass tube. The solution was then covered by 1 ml of methanol, followed by 4 ml of 0.1 M of $MnCl_2{\cdot}4H_2O$ (0.1 M) in methanol, and the glass tube was sealed. Polycrystalline powders $[(CH_3)_4N]Mn[N_3]_3$ were obtained after leaving the sealed glass tube undisturbed for three days.

X-ray diffraction data taken on the synthesized powder at atmospheric pressure and room temperature confirmed single-phase character (Fig. S1 of ESI†). Differential scanning calorimetry at atmospheric pressure (Fig. 1a) confirmed the first-order cubic-monoclinic phase transition at Th $\sim$ 309 K on heating

[a] *University of A Coruna, QuiMolMat Group, Dpt. Chemistry, Faculty of Science and Advanced Scientific Research Center (CICA), Zapateira, Coruña 15071 A, Spain. E-mail: m.senaris.rodriguez@udc.es, j.bermudez@udc.es*
[b] *Coordenação de Ciências Naturais, Universidade Federal do Maranhão, Campus do Bacabal, Bacabal, 65700-000, MA, Brazil*
[c] *Coordenação de Ciências Naturais, Universidade Federal do Maranhão, Campus VII, Codó, 65400-000, MA, Brazil*
[d] *Department of Materials Science, University of Cambridge, Cambridge CB3 0FS, UK. E-mail: xm212@cam.ac.uk*

† Electronic supplementary information (ESI) available: Powder X-ray diffraction spectra, isobaric entropy–temperature curves. See DOI: 10.1039/d0ma00652a

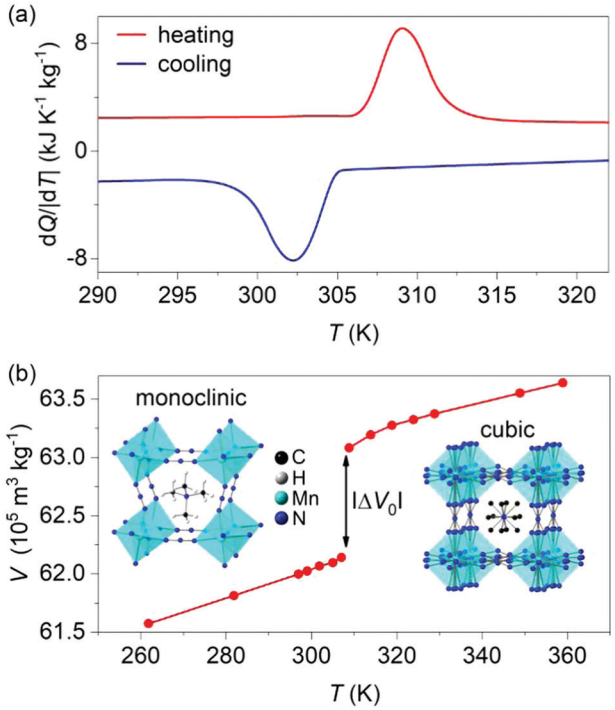

Fig. 1 (a) Heat flow $dQ/|dT|$ as a function of temperature, at atmospheric pressure. (b) Specific volume as a function of temperature, at atmospheric pressure, measured on heating *via* variable-temperature synchrotron powder X-ray diffraction. Left inset: pseudo-cubic representation of the low-temperature monoclinic phase; right inset: pseudo-cubic representation of the high-temperature cubic phase. H atoms in the high temperature phase are omitted for clarity of visualisation.

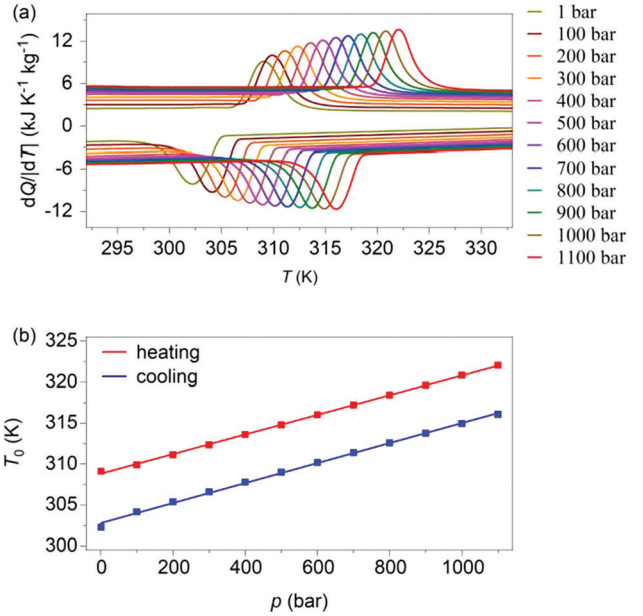

Fig. 2 (a) Heat flow $dQ/|dT|$ as a function of temperature, at finite applied pressures. (b) Transition temperatures *versus* pressure, identified using the peak in heat flow $dQ/|dT|$.

(identified using the peak in heat flow $dQ/|dT|$), and at $T_c \sim 302$ K on cooling (identified using the peak in heat flow $dQ/|dT|$), with a small thermal hysteresis of $\Delta T = T_h - T_c \sim 7$ K.

The thermally driven latent heat and entropy change for the transition (obtained *via* suitable integration[1,2] of the peaks in heat flow $dQ/|dT|$) where $|Q_0| = 25 \pm 1$ kJ kg^{-1} and $|\Delta S_0| = 80 \pm 1$ J K^{-1} kg^{-1}, respectively, in good agreement with literature values.[27,28]

The large values of $|Q_0|$ and $|\Delta S_0|$ arise primarily due to large changes in the degree of ordering[27] of the nitrogen atoms within the azide ligands (N_3), and of the monoclinic phase, $N = \exp(\Delta S_0/R)$, is 12 (R is the universal gas constant). When undergoing the phase transition from the monoclinic to the cubic phase, the azide N atoms get disordered over 4 different positions and the tetramethylammonium C atoms get disorder over twelve different positions.[27] This type of order–disorder phase transitions have been identified as mechanisms for potential barocaloric effects.[29]

Variable-temperature powder X-ray diffraction data (Fig. 1b) revealed a large increase in specific volume of $|\Delta V_0| \sim 9.40 \pm 0.03 \times 10^{-6}$ m^3 kg^{-1} on heating across the transition, which represents a relative change of $\sim$1.5%. The Clausius–Clapeyron equation $(dT_0/dp) = (\Delta V_0/\Delta S_0)$ returns a value of barocaloric tunability[25] dT_0/dp of $\sim 11.7 \pm 0.2$ K kbar^{-1} that is large but smaller than those obtained in dicyanamide perovskites.[24,25]

Variable-pressure differential scanning calorimetry (Fig. 2a) confirmed our calculated barocaloric tunability, with $dT_h/dp \sim dT_c/dp \sim 12$ K kbar^{-1} (Fig. 2b). Using these quasi-direct measurements,[1] we calculated pressure-driven isothermal changes in entropy (Fig. 3) by taking the difference between thermally driven changes in entropy measured at two different pressures (Fig. S2 of ESI†). Additional changes in isothermal entropy[17] that arise due to volumetric thermal expansion either side of the transition (Fig. 1a) were not considered because the coefficient of thermal expansion may decrease significantly under pressure for this compound.[30] These additional changes-if taken into account-will increase the magnitude of the here presented barocaloric effect, so the values of ΔS that we present are underestimated. We found giant isothermal changes in entropy $|\Delta S|$ of $\sim 33 \pm 1$ J K^{-1} kg^{-1} that can be driven reversibly using changes in applied pressure of $\sim$0.7 kbar. On increasing applied pressure further, we found $|\Delta S| \sim 70 \pm 1$ J K^{-1} kg^{-1} for $|p| \sim 1.1$ kbar, which is in agreement with a previous indirect prediction.[26]

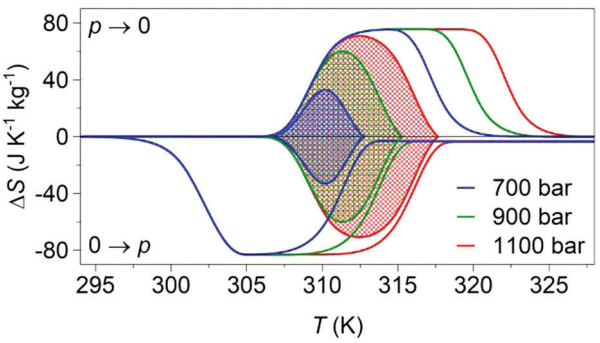

Fig. 3 Pressure-driven isothermal changes in entropy on applying ($0 \rightarrow p$) and removing ($p \rightarrow 0$) selected hydrostatic pressures. Data shaded using different colours represent the reversible[18] barocaloric response at different pressures.

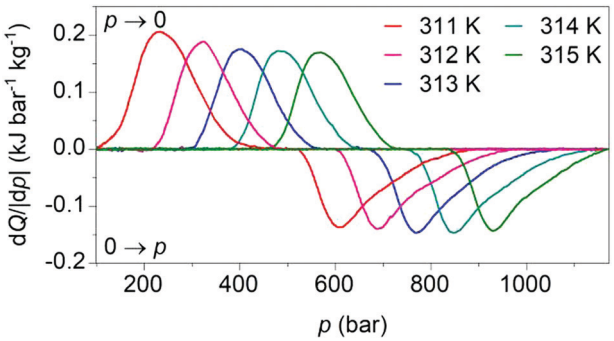

Fig. 4 Heat flow $dQ/|dp|$ on applying ($0 \rightarrow p$) and removing ($p \rightarrow 0$) hydrostatic pressure, after baseline subtraction, at different tempertures.

Our calculated pressure-driven changes in entropy were confirmed *via* direct measurements[1] of barocaloric heat (Fig. 4), which are rare, as few existing calorimeters permit the application of variable pressure. At 311 K, application and removal of ~900 bar drives reversibly our largest barocaloric entropy change of $|\Delta S| \sim 70 \pm 1$ J K^{-1} kg^{-1} (obtained *via* suitable integration of the peaks in heat flow $dQ/|dp|$). At higher temperatures, higher pressures are required to drive the transition reversibly but $|\Delta S|$ remains nominally constant. $[(CH_3)_4N]Mn[N_3]_3$ improves upon the performance of [TPrA]Mn[dca]$_3$ and [TPrA]Cd[dca]$_3$ dicyanamide perovskites (Table 1), by increasing twofold or more the barocaloric entropy change, and decreasing operating temperatures by ~25 K or more, at the expense of larger driving pressures.

The larger barocaloric entropy change arises due to the larger change in configurational order when driving the transition with pressure, *cf.* $N \sim 12$ for $[(CH_3)_4N]Mn[N_3]_3$, whereas it is ~8 and ~2.6 for the Mn-dicyanamide perovskite and the Cd-dicyanamide perovskite, respectively. The lower transition temperatures may arise due to a lower Goldschmidt tolerance factor, which is close to the ideal value of 1[31,32] for $[(CH_3)_4N]Mn[N_3]_3$. The higher driving pressure is a consequence of the smaller barocaloric tunability, $(dT_0/dp) = (\Delta V_0/\Delta S_0)$, as expected for systems with similar ΔV_0 but larger ΔS_0. Moreover, a larger thermal hysteresis also contributes to the need of a larger driving pressure for obtaining a reversible barocaloric effect upon cycling.

On the other hand, when comparing the azide perovskite with the best barocaloric organic and/or inorganic materials up to date, this perovskite exhibits a larger reversible barocaloric effect than most of the listed materials (except polyalcohols), with the advantage of working under lower pressures (Table 1).

In the future, it will be interesting to explore multicaloric effects[33] in this (and related) compounds, given that the monoclinc phase of $[(CH_3)_4N]Mn[N_3]_3$ is magnetic and antiferroelectric.[27]

Experimental methods

Caution

Azide compounds can be potentially explosive and should be handled with caution.

Sample synthesis

The following chemicals were used in the synthesis, as-purchased without further purification: $MnCl_2{\cdot}4H_2O$ (≥98%, Aldrich), $[(CH_3)_4N]Cl$ (purum ≥98%, Fluka), NaN_3 (≥99%, Aldrich), and CH_3OH (99.5%, Panreac).

Powder X-ray diffraction

Powder X-ray diffraction at room temperature was performed using a Siemens D-5000 diffractometer, with CuKα radiation (λ = 1.5418 Å). The recorded spectra was compared with an spectra that was simulated using existing single-crystal data and Mercury 3.5.1 software.

Variable-temperature powder X-ray diffraction using λ = 0.412483 Å at beamline BL04 – MSPD, Alba Synchrotron. For this experiment, ~5 mg of $[(CH_3)_4N][Mn(N_3)_3]$ were inserted in a borosilicate capillary of diameter ϕ = 0.5 mm, and the capillary was rotated during data collection. The recorded patterns were fitted using the Le Bail method.

Table 1 Comparison of the barocaloric parameters for the best hybrid, organic and inorganic barocaloric materials up to date

	Barocaloric material	T_0 (K)	$T_h - T_c$ (K)	$\lvert\Delta S_0\rvert$ (J kg^{-1} K^{-1})	$\lvert\Delta V_0\rvert$ 10^{-6} m^3 kg^{-1}	$\lvert dT_0/dp\rvert$ (K kbar^{-1})	$\lvert\Delta S\rvert$ (J K^{-1} kg^{-1})	Δp (bar)	Ref.
Hybrid	$[(CH_3)_4N]Mn[N_3]_3$	305	7	80	9.4	12	70	900	This work
	[TPrA]Mn[dca]$_3$	330	0.9	42.5	10	23.1	30.5	70	24
	[TPrA]Cd[dca]$_3$	386	1.4	16.2	5.3	38.2	11.5	70	25
Organics	$(CH_3)_2C(CH_2OH)_2$	311	25	372	46	10.3	445	2500	20
	$(CH_3)C(CH_2OH)_3$	354	12	482	38	8.7	490	2400	21
	$(CH_3)_3C(CH_2OH)$	251	33	200.5	45.5	17	290	2600	21
	Fullerite C_{60}	257	3	26.5	4.6	17	42	4100	23
Inorganics	$(NH_4)_2SO_4$	222	3	65	2.9	5.1	60	1000	17
	AgI	420	24	64	7.4	13.4	60	2500	18
	$Fe_{49}Rh_{51}$	314	10	12.5	1	5.9	12.5	2500	7
	$MnCoGeB_{0.03}$	290	18	47	5	10	30	1700	9

T_0 = transition temperature averaged from the peaks maximum on heating and cooling, $T_h - T_c$ = thermal hysteresis calculated from the peaks maximum on heating and cooling, $|\Delta S_0|$ = thermally driven entropy change averaged from peaks integration on heating and cooling, $|\Delta V_0|$ = volume change calculated on heating, $|dT_0/dp|$ = barocaloric tunability averaged from heating and cooling, $|\Delta S|$ = reversible pressure-driven isothermal entropy change obtained by quasi-direct methods, Δp = corresponding driving pressure for $|\Delta S|$.

Differential scanning calorimetry

Variable-pressure differential scanning calorimetry was performed using a Setaram μDSC7 EVO microcalorimeter equipped with a 260D Isco pressure pump that utilised nitrogen gas a pressure-transmitting media. Samples of ~100 mg of $[(CH_3)_4N][Mn(N_3)_3]$ were inserted in commercial pressure sample holders provided by Setaram and connected to the Isco pump. For quasi-direct barocaloric measurements, samples were swept in temperature at ±1.2 K min^{-1}. For direct barocaloric measurements, the same amount of sample was swept in pressure at ±10 bar min^{-1}.

Conflicts of interest

There are no conflicts of interest to declare.

Acknowledgements

The authors are grateful for financial support from Ministerio de Economía y Competitividad MINECO and EU-FEDER (MAT2017-86453-R), Xunta de Galicia (ED431G/09), FAMEPA (COOPI-07771/17), and ERC Starting Grant no. 680032. The authors acknowledge Alba Synchrotron beamline BL04 – MSPD. J. M. B. G. acknowledges Xunta de Galicia for a Postdoctoral Fellowship. X. M. and E. S. T. are grateful for support from the Royal Society.

Notes and references

1 X. Moya, S. Kar-Narayan and N. D. Mathur, *Nat. Mater.*, 2014, **13**, 439.
2 L. Mañosa and A. Planes, *Adv. Mater.*, 2017, **29**, 1603607.
3 S. Crossley, N. D. Mathur and X. Moya, *AIP Adv.*, 2015, **5**, 067153.
4 S. Yüce, M. Barrio, B. Emre, E. Stern-Taulats, A. Planes, J.-L. Tamarit, Y. Mudryk, K. A. Gschneidner Jr, V. K. Pecharsky and L. Mañosa, *Appl. Phys. Lett.*, 2012, **101**, 071906.
5 L. Mañosa, D. González-Alonso, A. Planes, M. Barrio, J.-L. Tamarit, I. S. Titov, M. Acet, A. Bhattacharyya and S. Majumdar, *Nat. Commun.*, 2011, **2**, 595.
6 L. Mañosa, D. González-Alonso, A. Planes, E. Bonnot, M. Barrio, J.-L. Tamarit, S. Aksoy and M. Acet, *Nat. Mater.*, 2010, **9**, 478–481.
7 E. Stern-Taulats, A. Planes, P. Lloveras, M. Barrio, J.-L. Tamarit, S. Pramanick, S. Majumdar, C. Frontera and L. Mañosa, *Phys. Rev. B: Condens. Matter Mater. Phys.*, 2014, **89**, 214105.
8 D. Matsunami, A. Fujita, K. Takenaka and M. Kano, *Nat. Mater.*, 2015, **14**, 73–78.
9 A. Aznar, P. Lloveras, J.-Y. Kim, E. Stern-Taulats, M. Barrio, J. L. Tamarit, C. F. Sánchez-Valdés, J. L. Sánchez-Llamazares, N. D. Mathur and X. Moya, *Adv. Mater.*, 2019, **31**, 1903577.
10 E. L. Rodriguez and F. E. Filisko, *J. Appl. Phys.*, 1982, **53**, 6536–6540.
11 I. N. Flerov, A. V. Kartashev, M. V. Gorev, E. V. Bogdanov, S. V. Mel'nikova, M. S. Molokeev, E. I. Pogoreltsev and N. M. Laptashf, *J. Fluorine Chem.*, 2016, **183**, 1–9.
12 M. Gorev, E. Bogdanov, I. N. Flerov, A. G. Kocharova and N. M. Laptash, *Phys. Solid State*, 2010, **52**, 167–175.
13 M. Gorev, I. N. Flerov, E. Bogdanov, V. N. Voronov and N. M. Laptash, *Phys. Solid State*, 2010, **52**, 377–383.
14 I. N. Flerov, M. V. Gorev, A. Tressaud and N. M. Laptash, *Crystallogr. Rep.*, 2011, **56**, 9.
15 E. Stern-Taulats, P. Lloveras, M. Barrio, E. Defay, M. Egilmez, A. Planes, J.-L. Tamarit, L. Mañosa, N. D. Mathur and X. Moya, *APL Mater.*, 2016, **4**, 091102.
16 Y. Liu, J. Wei, P.-E. Janolin, I. C. Infante, X. Lou and B. Dkhil, *Appl. Phys. Lett.*, 2014, **104**, 162904.
17 P. Lloveras, E. Stern-Taulats, M. Barrio, J.-L. Tamarit, S. Crossley, W. Li, V. Pomjakushin, A. Planes, L. Mañosa, N. D. Mathur and X. Moya, *Nat. Commun.*, 2015, **6**, 8801.
18 A. Aznar, P. Lloveras, M. Romanini, M. Barrio, J.-L. Tamarit, C. Cazorla, D. Errandonea, N. D. Mathur, A. Planes, X. Moya and L. Mañosa, *Nat. Commun.*, 2017, **8**, 1851.
19 J. Min, A. K. Sagotra and C. Cazorla, *Phys. Rev. Mater.*, 2020, **4**, 015403.
20 P. Lloveras, A. Aznar, M. Barrio, P. H. Negrier, C. Popescu, A. Planes, L. Mañosa, E. Stern-Taulats, A. Avramenko, N. D. Mathur, X. Moya and J.-L. Tamarit, *Nat. Commun.*, 2019, **10**, 1803.
21 A. Aznar, P. Lloveras, M. Barrio, P. Negrier, A. Planes, L. Mañosa, N. D. Mathur, X. Moya and J.-L. Tamarit, *J. Mater. Chem. A*, 2020, **8**, 639–647.
22 B. Li, Y. Kawakita, S. Ohira-Kawamura, T. Sugahara, H. Wang, J. Wang, Y. Chen, S. I. Kawaguchi, S. Kawaguchi, K. Ohara, K. Li, D. Yu, R. Mole, T. Hattori, T. Kikuchi, S.-I. Yano, Z. Zhang, Z. Zhang, W. Ren, S. Lin, O. Sakata, K. Nakajima and Z. Zhang, *Nature*, 2019, **567**, 506–510.
23 J. Li, D. Dunstan, X. Lou, A. Planes, L. Mañosa, M. Barrio, J.-L. Tamarit and P. Lloveras, *J. Mater. Chem. A*, 2020, DOI: 10.1039/D0TA05399F.
24 J. M. Bermúdez-García, M. Sánchez-Andújar, S. Castro-García, J. López-Beceiro, R. Artiaga and M. A. Señarís-Rodríguez, *Nat. Commun.*, 2017, **8**, 15715.
25 J. M. Bermúdez-García, S. Yáñez-Vilar, A. García-Fernández, M. Sánchez-Andújar, S. Castro-García, J. López-Beceiro, R. Artiaga, M. Dilshad, X. Moya and M. A. Señarís-Rodríguez, *J. Mater. Chem. C*, 2018, **6**, 9867.
26 J. M. Bermúdez-García, M. Sánchez-Andújar and M. A. Señarís-Rodríguez, *J. Phys. Chem. Lett.*, 2017, **8**, 4419.
27 L. C. Gómez-Aguirre, B. Pato-Doldán, A. Stroppa, L. M. Yang, T. Frauenheim, J. Mira, S. Yáñez-Vilar, R. Artiaga, S. Castro-García, M. Sánchez-Andújar and M. A. Señarís-Rodríguez, *Chem. – Eur. J.*, 2016, **22**, 7863–7870.
28 F. A. Mautner, S. Hanna, R. Cortés, L. Lezama, M. G. Barandika and T. Rojo, *Inorg. Chem.*, 2002, **38**, 4647–4652.
29 C. Cazorla, *Appl. Phys. Rev.*, 2019, **6**, 041316.
30 D. Walsh and P. Zoller, *Standard pressure volume temperature data for polymers*, CRC Press, 1995.
31 G. Kieslich, S. Sun and A. K. Cheetham, *Chem. Sci.*, 2015, **6**, 3430–3433.
32 J. M. Bermúdez-García, M. Sánchez-Andújar, S. Yáñez-Vilar, S. Castro-García, R. Artiaga, J. López-Beceiro, L. Botana, A. Alegría and M. A. Señarís-Rodríguez, *Inorg. Chem.*, 2015, **54**, 11680.
33 E. Stern-Taulats, T. Castán, L. Mañosa, A. Planes, N. D. Mathur and X. Moya, *MRS Bull.*, 2018, **43**, 295–299.

